On-the-fly adaptive SNR protocol to accelerate Brillouin microscopy

Léo Brechet, Valentin Gilet, Nizar Bouhlel, Matthieu Loumaigne, Cyril Ruckebusch, Nicolas Dobigeon, Li Zhang, Fabrizio Gala, Claudia Testi, Emanuele Pontecorvo, et al.

Research Article Vol. 33, No. 13 / 30 Jun 2025 / Optics Express 28511
Optics EXPRESS

On-the-fly adaptive SNR protocol to accelerate Brillouin microscopy

LÉO BRECHET,[1] VALENTIN GILET,[1] NIZAR BOUHLEL,[2] MATTHIEU LOUMAIGNE,[3] CYRIL RUCKEBUSCH,[4] NICOLAS DOBIGEON,[5] LI ZHANG,[6] FABRIZIO GALA,[6,7] CLAUDIA TESTI,[6] EMANUELE PONTECORVO,[6,7] GIANCARLO RUOCCO,[6] AND DAVID ROUSSEAU[1,*]

[1]*Université d'Angers, LARIS, UMR IRHS INRAe, F-49000, France*
[2]*Institut Agro Rennes-Angers, UMR 1345, F-49000, France*
[3]*Université d'Angers, MOLTECH-Anjou, UMR CNRS 6200, F-49000, France*
[4]*Université de Lille, CNRS, LASIRE, F- 59000 Lille, France*
[5]*Université de Toulouse, IRIT/INP-ENSEEIHT, 31071 Toulouse, France*
[6]*Center for Life Nano Science, Istituto Italiano di Tecnologia, Rome, Italy*
[7]*CrestOptics S.p.A., Via Di Torre Rossa, 66, 00165 Roma, Italy*
[*]*david.rousseau@univ-angers.fr*

Abstract: This article presents an innovative method for accelerating Brillouin microscopy imaging. The proposed technique, called One-pass, dynamically adjusts the signal-to-noise ratio (SNR) during data acquisition. It identifies essential spectra in real-time and adapts the laser exposure time accordingly. This approach considerably reduces acquisition time (by a factor around 2.2 and 3.5) while maintaining acceptable image quality, as demonstrated on simulations and real biological samples (HeLa and SK-N-SH cells). The method improves the stability and efficiency of Brillouin imaging compared with conventional techniques, i.e., raster scan with a single long exposure time or the recently introduced two-pass approach.

1. Introduction

Brillouin microscopy [1–4] has emerged as a powerful tool for the non-invasive mapping of mechanical properties in biological samples at the cellular resolution. A current limitation of the technique is the acquisition time which is not systematically compatible with real-time imaging of in vivo samples. This is intrinsically linked with the point-by-point raster-scanning of the sample. The resulting acquisition times can range from a few to tens of minutes for extended samples. Consequently, an open research front of Science aims at accelerating the data acquisition in Brillouin microimaging via computational approaches [5,6].

Some acceleration can be achieved via the instrumentation itself, e.g., involving line scanning [7–9] by laser pulse waveform shaping [10,11] or full-field systems [12,13]. Other advances in Brillouin signal enhancement have also been reported via interferometric filtering [14], or adaptive optics [15]. Apart from these physical approaches very few alternatives have exploited the spatial-spectral nature of the Brillouin hyperspectral images that exhibit strong redundancies both in the spatial and spectral domains [16–19]. So far, these computational alternatives [16–19] exploit the power of data to train machine learning algorithms and leverage on the expressiveness of these algorithms but can also suffer from the limitation of being valid only on the type of samples they have been trained on.

Recently, yet another approach combining spatial and spectral domain compression has allowed for a 1000-fold reduction in acquisition time in Raman micro-imaging [20]. The authors mentioned that their acquisition protocol can be extended to other hyperspectral microscopy. The approaches in [20] and the related contributions [21–23] assume that the spectral information of the sample can be recovered from only a few pixels of the hyperspectral image, whose spectral

#560295 https://doi.org/10.1364/OE.560295
Journal © 2025 Received 24 Feb 2025; revised 14 Apr 2025; accepted 24 Apr 2025; published 27 Jun 2025

Optics EXPRESS

signatures are called essential spectra. These essential spectra form a convex hull of the data points in a reduced space. We use the spectral phasor plane which is well-known in Brillouin spectroscopy and compatible with on-the-fly applications via simple fast Fourier transform [24]. This brings an important source of acceleration in the acquisition. The acquisition protocol of [20] was successfully extended to Brillouin synthetic images in [25].

So far, several passes are needed in the algorithm proposed in [20,25]. A first pass acquires the whole sample at low signal-to-noise ratio (SNR) and locates the essential spectra. A second pass is then needed to scan at high SNR the pixel corresponding to the essential spectra. This second pass is a limitation since it assumes that the scanning system is capable of pointing again to the same location or that the sample has not changed (spatially or spectrally). This paper considers yet a further extension of the algorithm proposed in [20,25] with a variant including only one pass while the SNR is adapted on-the-fly. The performance of this algorithm is assessed both on simulated and real data.

2. Material and methods

We describe in this Section all the ingredients of the proposed method and the real biological samples used to test it.

2.1. Brillouin microscope and standard acquision method

The Brillouin microscope used during the experiments is the setup depicted in Fig. 1 and is made of two main blocks. First, the beam block contains the laser and the filtering system. It is made of a Rubidium laser (780nm) which is filtered thanks to an etalon filter and a Bragg grating in a two-pass configuration. The second block performs the scan of the targeted sample. The standard acquisition method is based on a raster scan. The laser is moved across each region of the sample thanks to an external trigger that gives a clock signal to a piezoelectric which is connected to the stage. The spectromerter is based on a virtually images pased array (VIPA) [26] enabling high-throughput sub-GHz spectroscopy at a high finesse, with a nominal free spectral range of 15 GHz directing light, onto a CMOS sensor for a spectral resolution of 100MHz per pixel.. The exposure time on this detector is defined once for all at the beginning of the acquisition, and the data is dumped only once at the end to limit memory access. This standard raster scan method is made of 10 000 points with the set up of Fig. 1 which takes about 20 min for a single image. In this article, we propose an optimization of the scanning strategy to speed up this process while keeping the process on-the-fly and the quality of the Brillouin spectrum acquired almost unaffected.

2.2. Smart scanning protocols

The proposed One-pass acquisition method leverage on our recent innovative acquisition protocol [20]. We propose a variant of this acquisition protocol that allows a live update of the SNR, providing possibly different exposure time for each pixel, in contrast with a standard acquisition raster scan process. In this Section, we first provide a synthetic description of the protocol of [20] and then we detail our novel on-the-fly version.

2.2.1. Two-pass scan protocol adapted to Brillouin microscopy

Figure 2 illustrates our adapted smart scanning protocol, originally designed for Raman microscopy [20] and revisited here to suit Brillouin microscopy needs [25]. This two-step approach begins with a fast low-SNR acquisition of the entire sample yielding an hyperspectral image (HSI) $\mathrm{I}_{\mathrm{low}}(x, y, \lambda)$, a spectral cube comprising $X \times Y$ pixels across L wavelengths. Independently, dimensionality reduction is then applied along λ, resulting in a mono-component image $\mathrm{I}_{\mathrm{mono}}$. Such a dimension reduction can be done in many different ways. For Raman microscopy, several

Optics EXPRESS

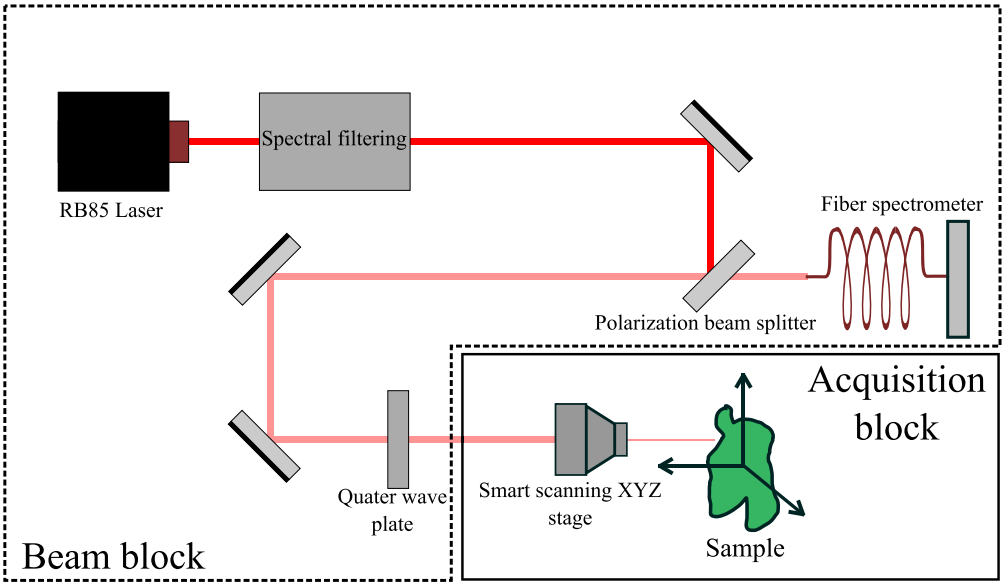

Fig. 1. Simple schema of the Brillouin microscope used.

standard dimension reduction techniques along λ (A simple mean, principal component analysis, UMAP,. . .) were, for instance, tested in [20]. One can also consider spectral indices (a simple ratio of two components selected at two distinc specific wavelength) as done in our recent work on bone tissues [27]. In Brillouin microscopy, the maximum energy is typically concentrated in the Rayleigh part of the spectrum, whereas the information of interest is contained in the Brillouin part of the spectrum, making these techniques ineffective. Instead, we defined a frequency range of interest based on the wavelength associated with one Brillouin peak and constructed a map of Brillouin shifts by fitting it to a Lorentzian function. Further processing involves segmenting this image into P superpixels using the Simple Linear Iterative Clustering algorithm, known as SLIC [28], producing $\mathrm{I}_{\mathrm{seg}}$. A subset of spectra can be retrieved from this segmented image by selecting the centroids (x_p, y_p) with p ranging between 1 and P. This spatial domain compression is complemented by another pipeline detailed in what follows.

A discrete Fourier transform (DFT) is applied in parallel to the hyperspectral image $\mathrm{I}_{\mathrm{low}}$ along the wavelength domain, decomposing each spectrum into elementary waves represented as

$$I_{\mathrm{low}}(x,y)_l = \frac{1}{L}\sum_{r=1}^{L}(G_r(x,y) + jQ_r(x,y))\exp\left(j\frac{2\pi}{L}(l-1)(r-1)\right), \tag{1}$$

where $G_r(x,y)$ and $Q_r(x,y)$ are real-valued components of the r-th phasor, and j is the imaginary unit. For a fixed r, the convex hull (C-H) of the point cloud formed by $G_r(x,y)$ and $Q_r(x,y)$ identifies the phasors corresponding to the most linearly dissimilar spectra, called essential spectra. These spectra are collected into a matrix $\mathbf{S}_{\mathrm{low}}$, with K essential spectra as rows and L spectral bands as columns, achieving spectral domain compression by retaining the most representative spectral information.

2.2.2. One-pass scan, on-the-fly proposed protocol

The Two-pass smart acquisition protocol of the previous subsection was successfully demonstrated on simulated Brillouin data in [25]. One limitation when transfering it to the real world is the need to come back exactly at the same location between the two passes of the scan. To overcome

Optics EXPRESS

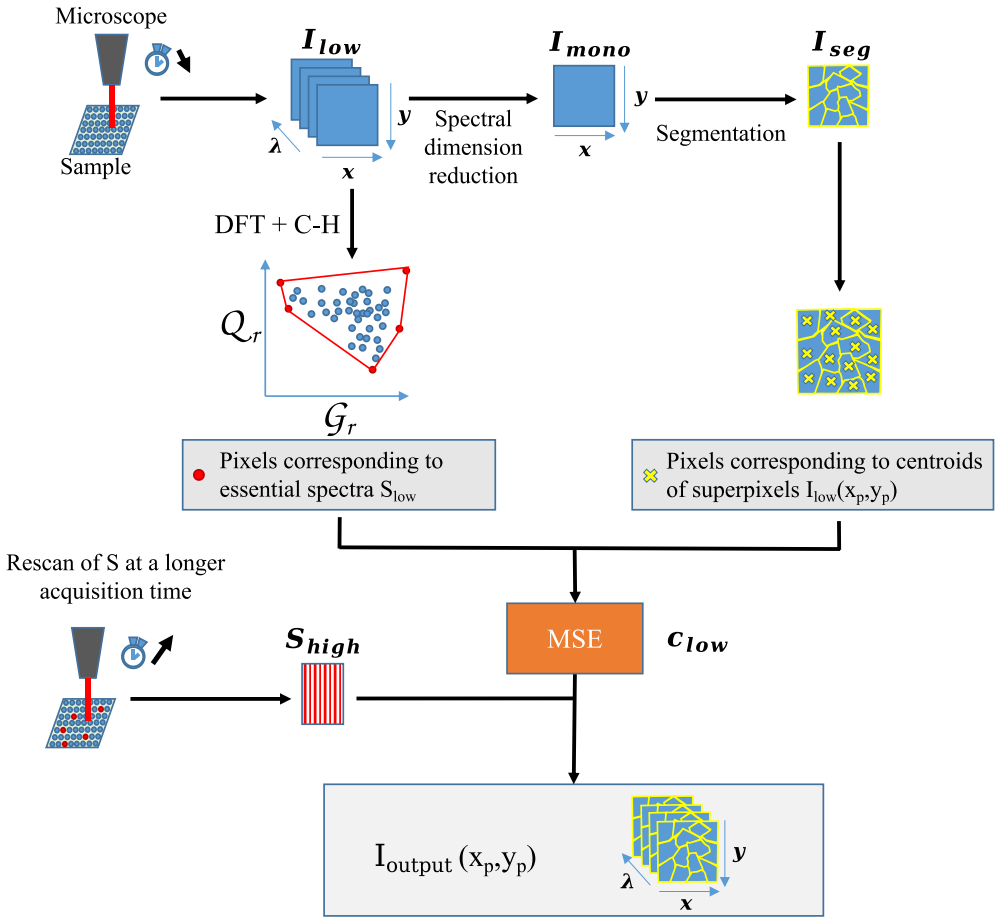

Fig. 2. Pipeline of the protocol proposed in [20] as recalled in Section 2.2.1 and Eq. (1).

this issue, we propose the following variant which includes only a single pass in the acquisition method as described in Fig. 3.

In the initialization step, the Brillouin spectra of the three first pixels of the sample are acquired at High SNR. These are used to initialize the computation of the convex hull of the point cloud represented by the simplest convex object, i.e. a triangle, set in the $G_r(x, y)$–$Q_r(x, y)$ phasor plane. These three measurements are saved once for all. Then, the core of the acquisition operates in two distinct modes.

(1) Mode 1: i.e.initial step: each pixel is first acquired at low SNR. Its location in the phasor plan is computed. If this phasor is located inside the convex hull that has been defined at the initialization step, the associated spectral mesurement is kept, and the acquisition process repeats on the next pixel. Else, if the phasor is located outside the convex hull, it is considered to carry some new spectral information, and the process goes into mode 2.

(2) Mode 2: the low SNR measurement is replaced by a high SNR acquisition. Last, the convex hull is computed again and updated with this new phasor and the acquisition process repeats on the next pixel in mode 1.

Optics EXPRESS

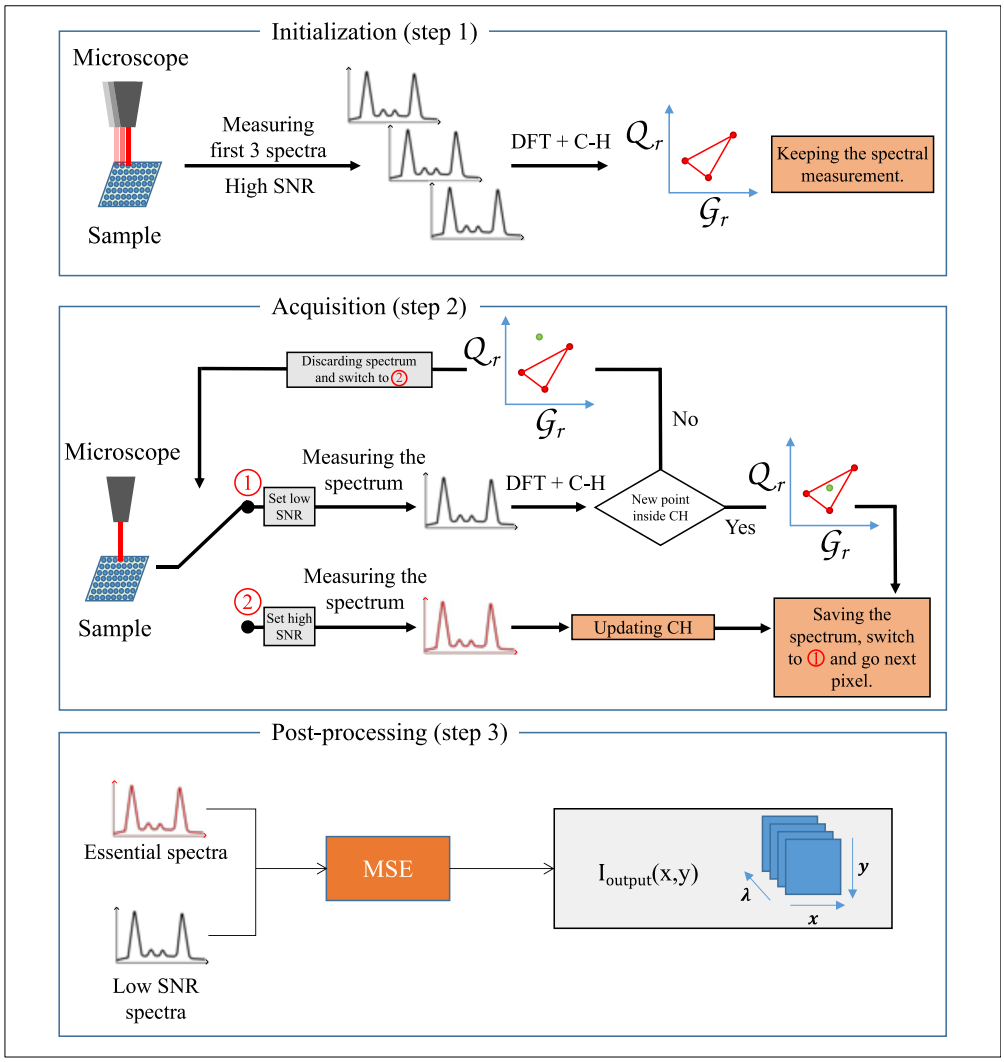

Fig. 3. Detailed view of the proposed One-pass adaptive SNR protocol proposed in Section 2.2.2.

Once all pixels are acquired at high or low SNR, the spectra of the pixels taken at low SNR are reconstructed based on the essential spectra i.e. the spectra corresponding to the vertices of the convex-hull in the phasor plane at final stage (as described in [20]).

The hypothesis behind this One-pass acquisition protocol is that the sample is expected to be spectrally redundant so that many pixels carry the same spectra. Therefore, if one spectra has already been seen it will already be included in the convex-hull. The performance of this One-pass algorithm is expected to be faster than a standard High-SNR raster scan and slower but of better quality than a Low-SNR raster scan. This is this trade-off we propose to quantity in the sequel of the article.

2.3. Data

We have tested our One-pass acquisition method, on two types of real samples that we describe here.

Optics EXPRESS

(1) HeLa cells [29] are a widely used cell line derived from human cervical cancer cells. These cells are remarkable for their ability to continuously divide and grow in culture, making them invaluable for research in cancer, virology, genetics, and various other biomedical fields. HeLa cells exhibit high proliferative capacity and have been instrumental in the development of numerous vaccines, cancer therapies, and medical advancements. Their immortality arises from mutations that bypass normal cell cycle controls, including the overexpression of telomerase, which maintains telomere length.

(2) SK-N-SH [29,30] is a human neuroblastoma cell line derived from a 4-year-old male patient with metastatic neuroblastoma, a cancer originating from neural tissue. These cells are widely used in research focused on neurobiology, cancer, and developmental biology due to their ability to differentiate into neurons under specific conditions. SK-N-SH cells express markers typical of neuroblastoma and exhibit various properties of neuronal cells, including the production of neurotransmitters and the formation of neural networks when induced to differentiate. They are often used to study neuroblastoma pathophysiology, drug screening, and neurodegenerative diseases. Like many immortalized cell lines, SK-N-SH cells exhibit an enhanced growth rate and altered genetics, which allows for extended culture periods and reproducible experiments.

2.4. Simulation

We created a simulator of the two real data set described in the previous Section to further extend the range of investigation. The two types of cell can be viewed as made of three regions of interest: the nucleus (containing the nucleoli), the cytoplasm, and the matrix (water here). The spectrum of each of these materials is made of a Rayleigh peak and a Brillouin peak. These spectral peaks are classically modeled as an Asymmetric Pseudo-Voigt [31] which reads

$$R(\nu, \nu_R, H_R, \alpha_1, \alpha_2, w_R) = \begin{cases} H_R \times \left(\alpha_1 \, \mathcal{L}(\nu, \nu_R, w_R) + (1-\alpha_1)\, \mathcal{N}(\nu, \nu_R, w_R)\right) \; ; \; \nu < \nu_R \\ H_R \times \left(\alpha_2 \, \mathcal{L}(\nu, \nu_R, w_R) + (1-\alpha_2)\, \mathcal{N}(\nu, \nu_R, w_R)\right) \; ; \; \nu \geq \nu_R \end{cases} , \quad (2)$$

with ν the frequency, ν_R the location of the peak, H_R the height of the peak, w_R the width of the peak,

$$\mathcal{N}(\nu, F, W) = e^{-\ln 2\left(\frac{\nu - F}{W/2}\right)^2} \quad (3)$$

a Gaussian function,

$$\mathcal{L}(\nu, F, W) = \frac{1}{1 + \left(\frac{\nu - F}{W/2}\right)^2} \quad (4)$$

a Lorentzian function and α_1 (resp α_2) the fraction of the Lorentzian in the left part (resp. the right part) of the Pseudo-voigt, and a Lorentzian bell

$$B(\nu, \nu_B, H_B, w_B) = H_B \, \mathcal{L}(\nu, \nu_B, w_B) \, , \quad (5)$$

with ν_B the Brillouin frequency, H_B the Brillouin intensity and w_B the Brillouin peak full width at half maximum (FWHM).

These spectral information are further corrupted with a classical thermal noise which can be modeled as an independent and identically distributed Gaussian noise. The simulator of Brillouin microscopy data described above was tuned to fit with data from real samples. As real samples, we used cells of HeLa and SK-N-SH cells imaged with various objectives (x20, x40, x60). To excite the sample, a 780 nm Rubidium laser was used. The diffuse light emitted by the sample was then split with a virtually imaged phased array (VIPA) device and collected by a

Optics EXPRESS

complementary metal-oxide-semiconductor (CMOS) sensor. Several replicated measurements at different acquisition times were performed to study the relation between the signal-to-noise ratio

$$\mathrm{SNR} = 10\log_{10}\left(\frac{I}{\sigma_N}\right), \tag{6}$$

that we defined as the ratio of the maximum intensity of the Brillouin peak I and the standard deviation of the noise σ_N, and the acquisition time. These multiple acquisitions allowed us to estimate t_{exp}, the exposure time of each measurement. The similarity of the real and generated data are shown in Fig. 4 both in the spectral and spatial domain. One can recognize the Rayleigh peaks at 0 and 15 GHz, the Brillouin anti-Stokes peaks at 5 and 20 GHz and the Brillouin Stokes peaks at −5 and 10 GHz. Multiple Rayleigh and Brillouin peaks appear on the spectrum due to the narrow free spectral range of the used VIPA interferometer. The Brillouin peak of interest for the extraction of mechanical properties is the anti-Stokes of the first order, spotted here around 5 GHz. The Brillouin shift for each component of the cells is provided in Fig. 4. On the real spectra one, the Rayleigh peaks do not have the same amplitude. This is due to the position of the frequency of the laser cavity which may not be centered on the part of interest of the spectra. As visible in Fig. 2, we choose not to include this aspect in our simulator.

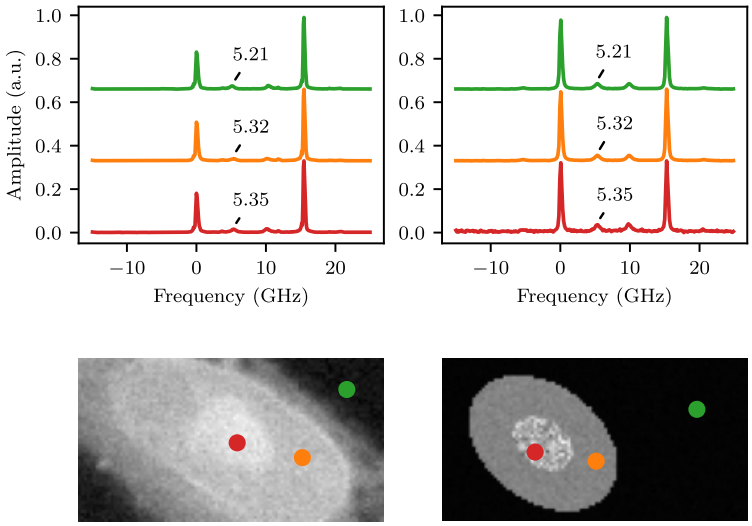

Fig. 4. Spatial and spectral comparisons of a real and a simulated cell. Both have been normalized between 0 and 1 to exhibit the similarity.

The detail of parameters H_B, ν_B and w_B which have been used to build the synthetic data through Eq. (2) and Eq. (5) are provided in Table 1. The synthetic dataset has been composed of 90 spectral cube of the same simulated sample at different SNR, ranging from 5 dB to 24 dB in order to assess the robustness and the gain in time of the protocol. To provide an estimation of the noise-induced variance, we replicated the same spectral cube five times for each SNR. The spectral cube corresponding to the SNR of 24 dB was chosen as High SNR reference for assessment. We note this reference as $\boldsymbol{I}_{\mathrm{ref}}$ and this reference was used to simulate the second pass at a higher SNR. Thus, we collected $\boldsymbol{S}_{\mathrm{high}}$ from this reference.

2.5. Evaluation metrics

To evaluate the reconstruction of the spectral cube by the protocols described in Section 2.2, we decided to focus on the assessment of the restitution of the anti-Stokes Brillouin peak of the

Optics EXPRESS

first order across the entire HSI. Its characterization is indeed essential to study the composition of the sample since it carries most of its mechanical properties. Thus, for each pixel of the reconstructed spectral cube, we computed the mean absolute error (MAE) of the shift

$$\nu_{\text{err}} = \frac{1}{XY}\sum_{x=1}^{X}\sum_{y=1}^{Y}|\nu_B(x,y) - \nu_{\text{ref}}(x,y)|, \tag{7}$$

and of the FWHM

$$w_{\text{err}} = \frac{1}{XY}\sum_{x=1}^{X}\sum_{y=1}^{Y}|w_B(x,y) - w_{\text{ref}}(x,y)|, \tag{8}$$

with $\nu_B(x,y)$ and $w_B(x,y)$ the Brillouin shift and FWHM estimated on $\boldsymbol{I}_{\text{output}}(x,y)$, and $\nu_{\text{ref}}(x,y)$ and $w_{\text{ref}}(x,y)$ estimated on $\boldsymbol{I}_{\text{ref}}(x,y)$ by fitting Eq. (5) on the reconstructed data using least mean square method.

MAE has been chosen to penalize outliers. Furthermore, we evaluated the processing time of the entire acquisition process, encompassing the time required for acquiring $\boldsymbol{I}_{\text{low}}$, and the rescan of the essential spectra $\boldsymbol{S}_{\text{high}}$.

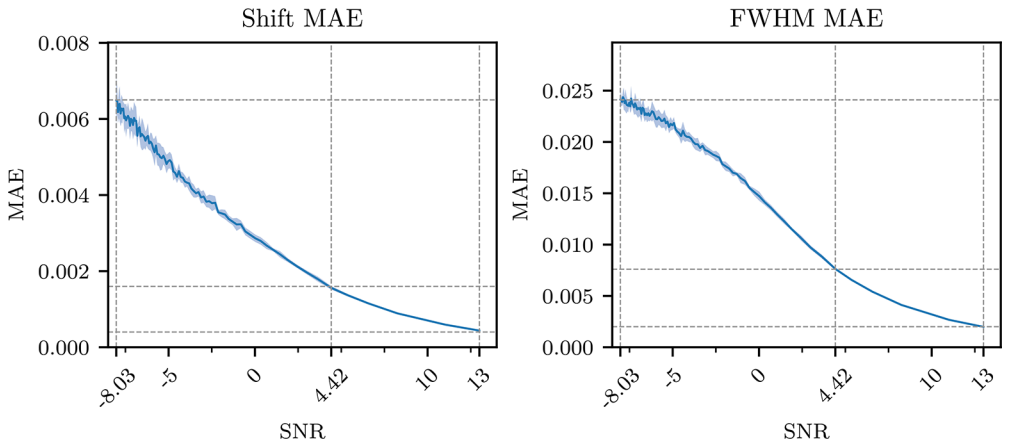

Fig. 5. Evolution of the MAE on the Brillouin shift and the FWHM on entire simulated images as a function of the Low-SNR. The translucent blue patch is the standard devation range computed over 10 repetitions of the simulation, and the dashed lines spot the values of interest from Table 2.

3. Results

We start with the assessment of the proposed One-pass acquisition protocol on simulated data. The quantitative results are provided in Fig. 5 and Table 2 for various values of Low-SNR. The reference is the standard High-SNR protocol. The error observed on the Brillouin shift ν_{err} and the FWHM w_{err}, that we assess from a mean absolute error, trivially degraded as the Low-SNR decreases. The recorded error amplitudes appear small in absolute amplitude. However, one has to relate these amplitudes with the expected difference between each material composing the sample itself provided in Table 1. Indeed, Table 1 indicates a minimum difference of 0.10 GHz between the standard ν_B values of the different material composing our simulated sample. Interestingly, even at $SNR = 4.42$, ν_{err} reaches only 0.001, i.e. two orders of magnitude smaller than the difference between materials in terms of Brillouin shift in the simulated cells. This means that even at this low SNR a distinction between the materials should be possible. The

Optics EXPRESS

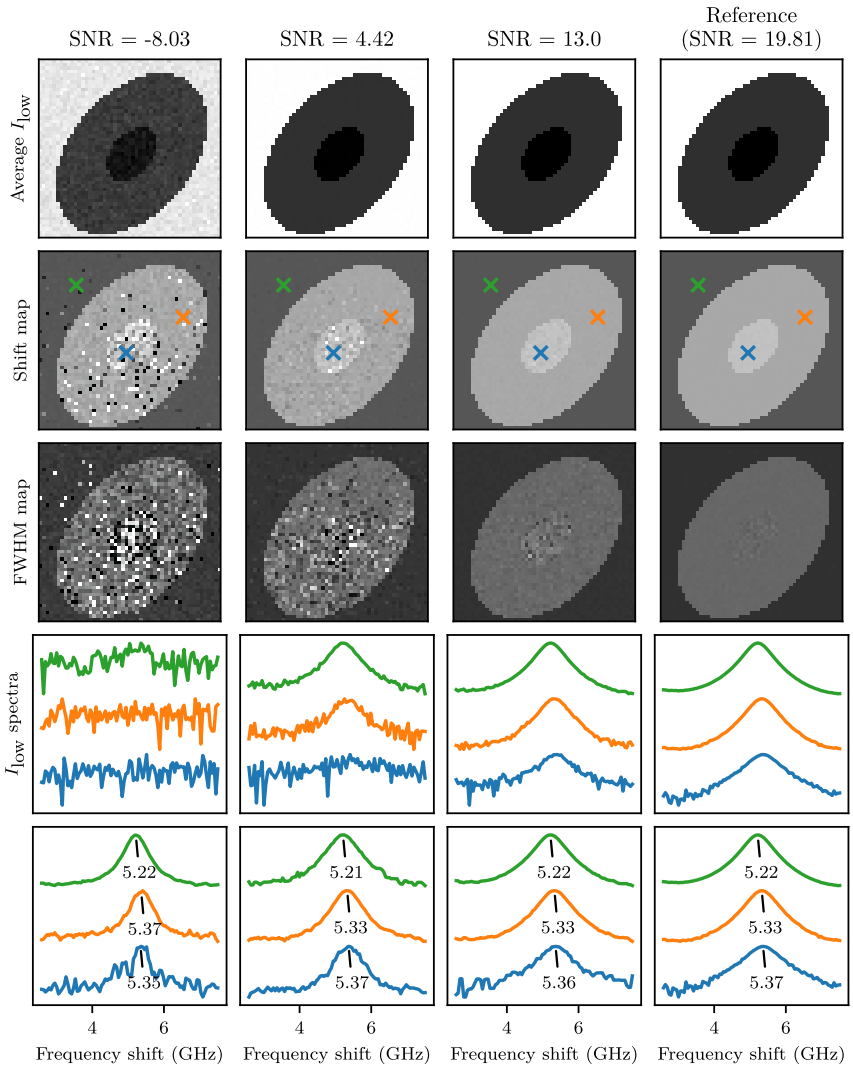

Fig. 6. Visual assesment of the One-pass reconstruction method at different values of SNR for simulated cells.

error becomes much larger at $SNR = -8$ but not large enough to produce confusion between the different materials that compose the cells. However, the lower the SNR, the more the spectra are challenging to fit. This involves a lot of outliers as visible in Fig. 6. These outliers make the identification of the material impossible without involving post-processing. A simple median filter here could help a lot but such a post-processing step falls out of the scope of this work. Table 2 exhibits the global exposure time for a set of low SNR. At SNR 13.00, the exposure time is reduced by a factor 2.4 by comparison with the standard full High-SNR acquisition protocol. A comparison with the Two-pass protocol of [20] and recalled in Fig. 3 is also provided in Table 2. With this Two-pass scanning protocol, the pixel providing the essential spectra are predetected (in a first pass) and only these pixels are rescanned at high SNR. Therefore, as expected, the Two-pass scan is faster than the One-pass algorithm but also provides larger error on the estimation of the Brillouin parameters.

Optics EXPRESS

Table 1. Estimated values of the Lorentzian curve, corresponding to the Brillouin peak on the real data. ν_B and w_B are in GHz, H_B in arbitrary unit.

	H_B	ν_B	w_B
Nucleus and nucleoli	63.0	5.36	0.86
Cytoplasm	291	5.33	0.85
Matrix, i.e. water	1391	5.22	0.79

Table 2. Summary table of the results on simulated data. The errors were calculated for simulated data after 10 repetitions.

Simulated cells	SNR	Total exposure time (s)	Metrics	
		(100 × 100 pixels image)	ν_{err} (GHz)	w_{err} (GHz)
One pass	13.00	415 ± 9	$(438 \pm 6)10^{-6}$	$(172 \pm 3)10^{-5}$
	4.42	734 ± 10	$(156 \pm 4)10^{-5}$	$(731 \pm 11)10^{-5}$
	−8.03	950 ± 2	$(64 \pm 6)10^{-4}$	$(238 \pm 11)10^{-4}$
Two pass	13.00	209.77 ± 0.021	$(227 \pm 5)10^{-5}$	$(99 \pm 8)10^{-4}$
	4.42	30.32 ± 0.8	$(80 \pm 8)10^{-4}$	$(83 \pm 11)10^{-4}$
	−8.03	3.03 ± 0.1	$(18 \pm 1)10^{-3}$	$(4 \pm 3)10^{-2}$
Reference	19.81	1000		

As a complement to the quantitative assessment of our method, we propose in Fig. 6 a qualitative visual appreciation of the results provided after estimation of the Brillouin spectra. The estimated spectra show a good quality on the Brillouin part even at low SNR (at least down to the lowest value 4.42 SNR tested in practice) thanks to the use of essential spectra. Since the One-pass protocol is on-the-fly it is interesting to visualize its evolution as a function of time. Figure 7 provides the cumulative acquisition time as a function of the number of measures. The One-pass one-the-fly proposed protocol with its adaptive SNR shows a behavior which is, as expected, in-between the High-SNR used for the pixel detected as essential and the Low-SNR used for the pixel detected inside the convex-hull drawn by the essential pixels. At the beginning of the process, all pixels are detected as essential and the slope of the cumulative time follows a pure standard High-SNR protocol. As the acquisition proceeds, the diversity of the sample is probed, the slope of the cumulative time decreases and appears more similar to the low-SNR. All new pixels are detected as part of the convex-hull of the essential pixels, there is no spectral novelty and only the low-SNR is used.

At last we tested the proposed One-pass protocol on the real samples used as reference for the simulation so far. The quantitative measurements provided in Table 3 and 4 are in accordance with the simulated data of Table 2 on the range of SNR accessible on our optical setup. An example of the two types of cells is provided in Figs. 8 and 9. For comparison, the Low-SNR and High-SNR protocol are also provided in these Figures. Spatially and spectrally the One-pass results appear close to the High-SNR with less distorsion than in the Low-SNR and an acquisition time which is here two times faster approximately.

Optics EXPRESS

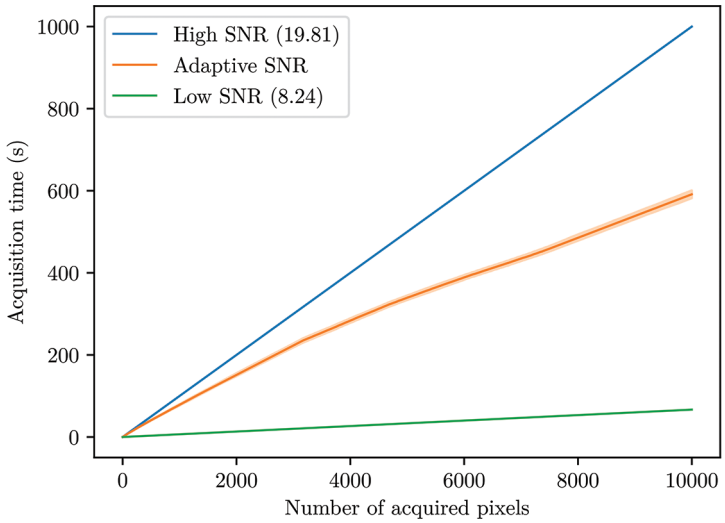

Fig. 7. Cumulated acquisition time as a function of the number of pixels measured for the proposed One-pass adaptive SNR protocol (in orange). The standard single SNR raster scan with High-SNR (in blue) and Low-SNR (in Green) is provided for comparison.

Table 3. Summary table of the results on HeLa real data. The error corresponding to an SNR of 12.82 was calculated from 3 images, and the error for an SNR of 14.58 was calculated from 10 images.

HeLa cells	SNR	Total exposure time (s)	Metrics	
		(100 × 100 pixels image)	ν_{err} (GHz)	w_{err} (GHz)
One pass	14.16	285 ± 36	0.07 ± 0.04	0.28 ± 0.10
	14.67	410 ± 36	0.02 ± 0.02	0.1 ± 0.1
Two pass	14.16	202.45 ± 0.03	0.09 ± 0.05	0.22 ± 0.09
	14.67	301.12 ± 0.05	0.04 ± 0.03	0.13 ± 0.011
Reference	18.16	1000		

Table 4. Summary table of the results on SK-N-SH real data. The error corresponding to an SNR of 12.82 was calculated from 9 images, and the error for an SNR of 14.58 was calculated from 5 images.

SK-N-SH cells	SNR	Total exposure time (s)	Metrics	
		(100 × 100 pixels image)	ν_{err} (GHz)	w_{err} (GHz)
One pass	13.75	455 ± 128	0.02 ± 0.02	0.05 ± 0.05
	14.68	371 ± 30	0.010 ± 0.012	0.04 ± 0.04
Two pass	13.75	203.81 ± 0.06	0.10 ± 0.05	0.11 ± 0.07
	14.68	302.76 ± 0.08	0.06 ± 0.08	0.06 ± 0.04
Reference	17.80	1000		

Optics EXPRESS

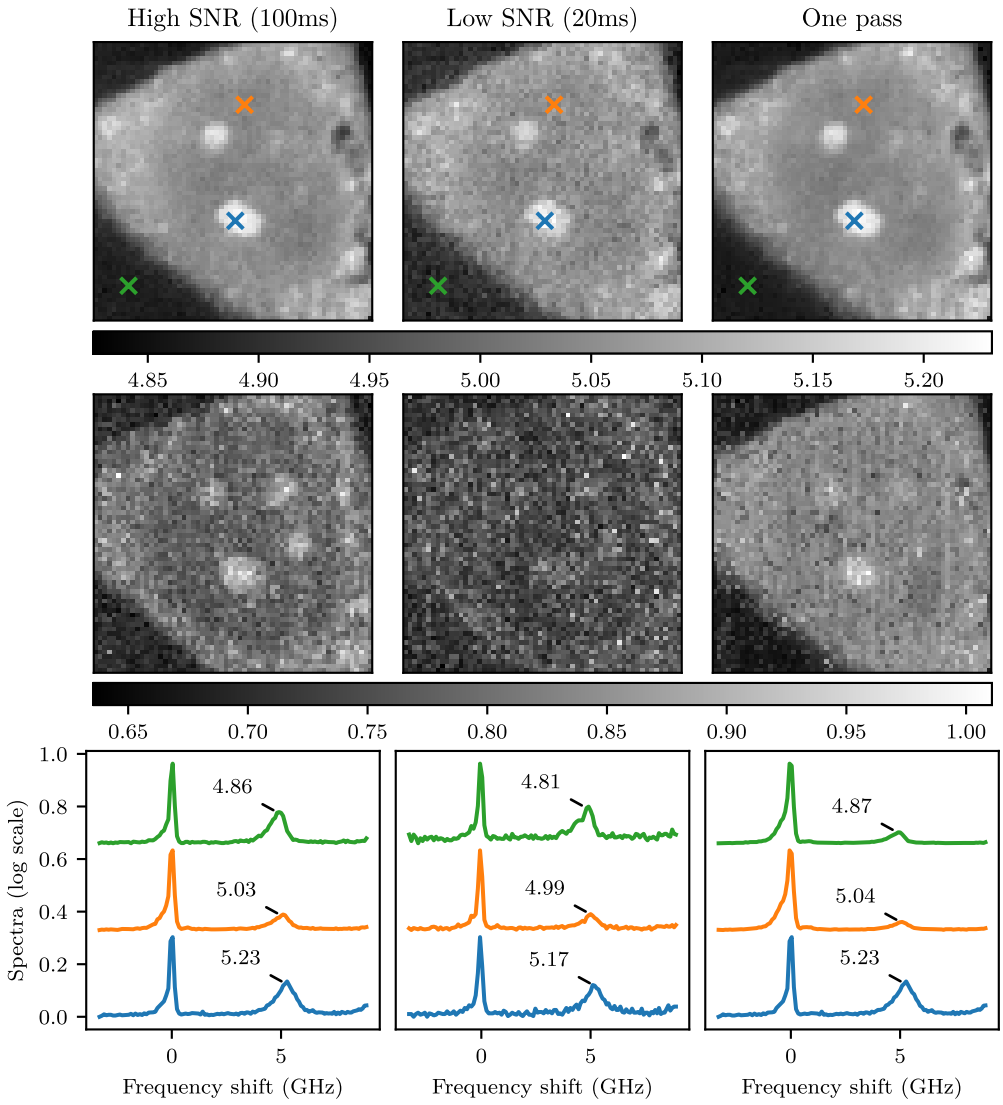

Fig. 8. Qualitative assessment of the adaptive SNR method on a real SK-cells sample. On the top, the Brillouin shift maps of the sample at two values of SNR, in the middle, the Brillouin peak FWHM and on the bottom the corresponding spectra (containing the first order Rayleigh peak and Brillouin anti-Stokes peak). The total exposure times are 6 min at high SNR, 1 min 12 at low SNR and 3 min 13 for the one pass. The image is 19.5 μm by 19.5 μm.

Optics EXPRESS

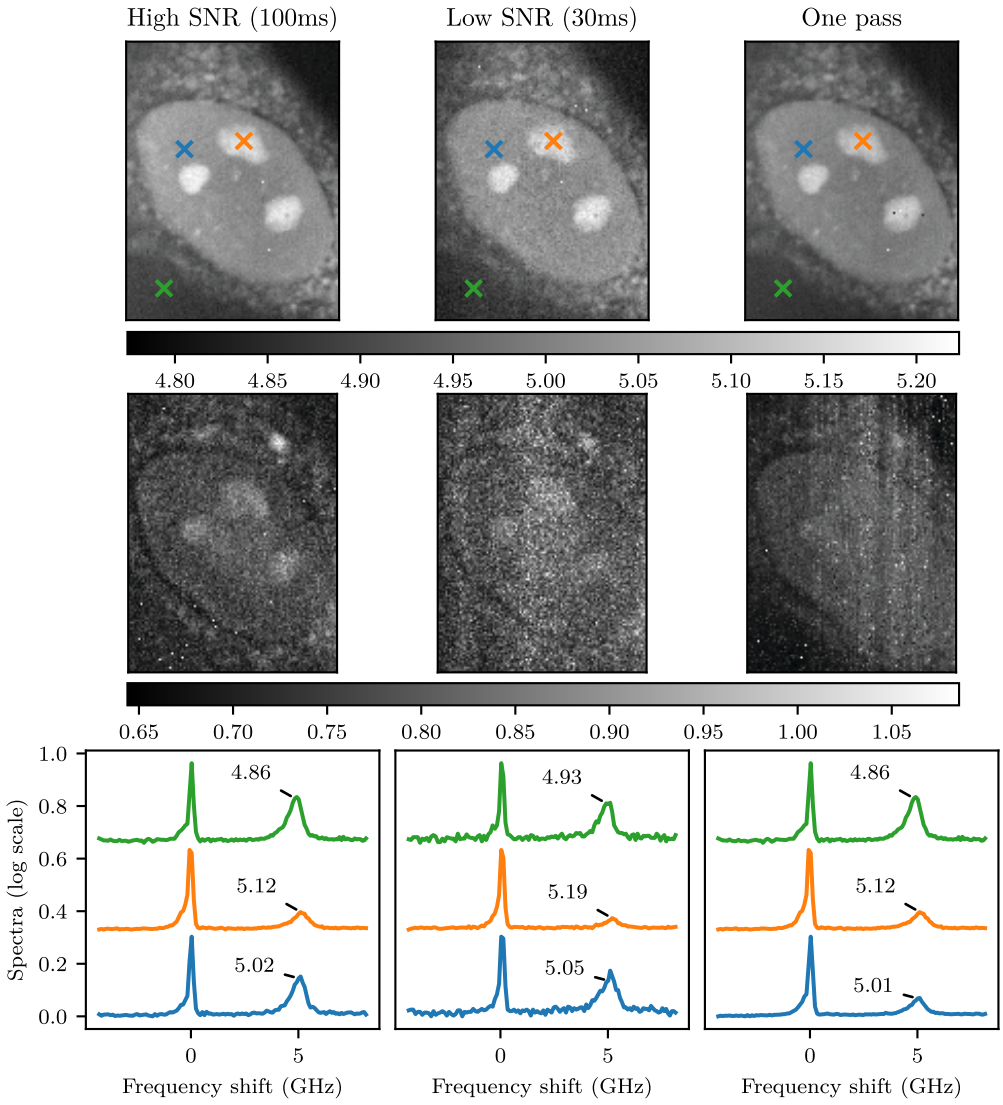

Fig. 9. Qualitative assessment of the adaptive SNR method on a real HeLa-cells sample. On the top, the shift maps of the sample at 2 values of SNR, in the middle, the Brillouin peak FWHM and on the bottom the corresponding spectra (containing the first order Rayleigh peak and Brillouin anti-Stokes peak). The total exposure times are 23 min 34 at high SNR, 7 min 04 at low SNR and 8 min 28 for the one pass. The image is 29.5 μm by 22.5 μm.

Optics EXPRESS

4. Conclusion

In this article we extended a recently introduced Two-pass smart scanning algorithm for Brillouin microscopy to a One-pass on-the-fly adaptive version. It was illustrated on simulated and real samples of clinical interest for Brillouin imaging. An acceleration factor of around 2.2 and 3.5 was recorded by comparison with standard High SNR protocol at a price of very limited distorsion. This acceleration is smaller than the factor 3 estimated with the Two-pass smart scanning algorithm previously presented in the literature for Brillouin and Raman microscopy as there is no compression in the spatial domain. The advantage of the proposed One-pass method is that, by design, it is one-the-fly and therefore depends less on the stability of the optical setup or the biological sample.

This proof of feasibility opens several new directions. First, the method is clearly sample dependent. A very redundant, i.e. self similar, sample will be more compressed than a very spatially and /or spectrally heterogeneous sample [32]. A systematic quantification of this aspect would be interesting to investigate on a large variety of samples of biological interest. This is specially accessible with the simulation setup developed for this study and that we make available to the reader (see Code 1, [33] available as supplementary material). The quantitative estimation limit of the method in terms of Cramer Rao bounds of the Brillouin parameters would be also worth investigating theoretically. This is also accessible with the parametric model proposed in this article with the possibilities of analytical closed form expression also in the phasor domain as stressed in [24].

Last, the proposed on-the-fly adaptive SNR protocol, illustrated here on Brillouin, could be extended to other point-by-point spectral imaging methods for which acceleration could be targeted. For instance, one could think of near infrared spectroscopy or also Tera-Herz spectroscopy.

Acknowledgements. This project has received funding from the European Innovation Council through its Horizon Europe Pathfinder Programme under grant agreement No 101098989. Funded by the European Union. Valentin Gilet, Nicolas Dobigeon, Cyril Ruckebusch, David Rousseau also gratefully acknowledge financial support from the "ANR-21-CE29-0007" project (Agence Nationale de la Recherche).

Disclosures. The authors declare no conflicts of interest.

Data availability. Code for the Brillouin spectra simulator is available in Code 1 [33]. Data underlying the results presented in this paper are not publicly available at this time but may be obtained from the authors upon reasonable request.

References

1. R. Prevedel, A. Diz-Muñoz, G. Ruocco, *et al.*, "Brillouin microscopy: an emerging tool for mechanobiology," Nat. Methods **16**(10), 969–977 (2019).
2. C. Wolff, M. J. A. Smith, B. Stiller, *et al.*, "Brillouin scattering—theory and experiment: tutorial," J. Opt. Soc. Am. B **38**(4), 1243 (2021).
3. C. Handler, C. Testi, and G. Scarcelli, "Advantages of integrating Brillouin microscopy in multimodal mechanical mapping of cells and tissues," Curr. Opin. Cell Biol. **88**, 102341 (2024).
4. I. Kabakova, J. Zhang, Y. Xiang, *et al.*, "Brillouin microscopy," Nat. Rev. Methods Primers **4**(1), 8 (2024).
5. G. Antonacci, T. Beck, A. Bilenca, *et al.*, "Recent progress and current opinions in Brillouin microscopy for life science applications," Biophys. Rev. **12**(3), 615–624 (2020).
6. A. Bilenca, R. Prevedel, and G. Scarcelli, "Current state of stimulated Brillouin scattering microscopy for the life sciences," J. Phys. Photonics **6**(3), 032001 (2024).
7. J. Zhang, A. Fiore, J. Zhang, *et al.*, "Line-scanning Brillouin microscopy for rapid non-invasive mechanical imaging," Sci. Rep. **6**(1), 35398 (2016).
8. J. Zhang, M. Nikolic, K. Tanner, *et al.*, "Rapid biomechanical imaging at low irradiation level via dual line-scanning Brillouin microscopy," Nat. Methods **20**(5), 677–681 (2023).
9. N. Khalilgharibi, G. Paci, and Y. Mao, "Line-scanning speeds up Brillouin microscopy," Nat. Methods **20**(5), 643–644 (2023).
10. B. Krug, N. Koukourakis, and J. W. Czarske, "Impulsive stimulated Brillouin microscopy for non-contact, fast mechanical investigations of hydrogels," Opt. Express **27**(19), 26910–26923 (2019).
11. F. Yang, C. Bevilacqua, S. Hambura, *et al.*, "Pulsed stimulated Brillouin microscopy enables high-sensitivity mechanical imaging of live and fragile biological specimens," Nat. Methods **20**(12), 1971–1979 (2023).

Optics EXPRESS

12. G. Scarcelli, R. Hutchins, and G. Zanini, "Full-field Brillouin microscopy systems and methods," (2024). US Patent 12,019,018.
13. C. Bevilacqua and R. Prevedel, "Full-field Brillouin microscopy based on an imaging Fourier transform spectrometer," arXiv (2024).
14. G. Lepert, R. M. Gouveia, C. J. Connon, *et al.*, "Assessing corneal biomechanics with Brillouin spectro-microscopy," Faraday Discuss. **187**, 415–428 (2016).
15. E. Edrei, G. Scarcelli, and G. Scarcelli, "Brillouin micro-spectroscopy through aberrations via sensorless adaptive optics," Appl. Phys. Lett. **112**(16), 163701 (2018).
16. B. Wang, N. Guo, L. Wang, *et al.*, "Robust and fast temperature extraction for Brillouin optical time-domain analyzer by using denoising autoencoder-based deep neural networks," IEEE Sens. J. **20**(7), 3614–3620 (2020).
17. Y. Xiang, K. L. C. Seow, C. Paterson, *et al.*, "Multivariate analysis of Brillouin imaging data by supervised and unsupervised learning," J. Biophotonics **14**(7), e202000508 (2021).
18. M. Alunni Cardinali, M. Govoni, M. Tschon, *et al.*, "Brillouin–Raman micro-spectroscopy and machine learning techniques to classify osteoarthritic lesions in the human articular cartilage," Sci. Rep. **13**(1), 1690 (2023).
19. Z. Sun, Y. Zhang, and Y. Lu, "Fast Brillouin optical time domain sensing based on two-dimension sparse sampling and deep learning recovery," Opt. Commun. **552**, 130043 (2024).
20. V. Gilet, G. Mabilleau, M. Loumaigne, *et al.*, "Superpixels meet essential spectra for fast Raman hyperspectral microimaging," Opt. Express **32**(1), 932–948 (2024).
21. L. Coic, P.-Y. Sacré, A. Dispas, *et al.*, "Pixel-based Raman hyperspectral identification of complex pharmaceutical formulations," Anal. Chim. Acta **1155**, 338361 (2021).
22. L. Coic, P.-Y. Sacre, A. Dispas, *et al.*, "Selection of essential spectra to improve the multivariate curve resolution of minor compounds in complex pharmaceutical formulations," Anal. Chim. Acta **1198**, 339532 (2022).
23. L. Coic, R. Vitale, M. Moreau, *et al.*, "Assessment of essential information in the Fourier domain to accelerate Raman hyperspectral microimaging," Anal. Chem. **95**(42), 15497–15504 (2023).
24. K. Elsayad, "Spectral phasor analysis for Brillouin microspectroscopy," Front. Phys. **7**, 62 (2019).
25. L. Brechet, V. Gilet, M. Loumaigne, *et al.*, "On the use of spatial and spectral redundancy to speed-up Brillouin micro-imaging," in *2024 32nd European Signal Processing Conference (EUSIPCO)*, (IEEE, 2024), pp. 621–625.
26. M. Shirasaki, "Virtually imaged phased array," Fujitsu Scientific & Technical Journal **35**, 113–125 (1999).
27. V. Gilet, G. Mabilleau, M. Loumaigne, *et al.*, "Dual-modality sem-raman smart scanning for fast hyperspectral raman micro-imaging–application to bones," Biomed. Opt. Express **16**(3), 935–948 (2025).
28. R. Achanta, A. Shaji, K. Smith, *et al.*, "Slic superpixels compared to state-of-the-art superpixel methods," IEEE Trans. Pattern Anal. Mach. Intell. **34**(11), 2274–2282 (2012).
29. J. L. Biedler, J. L. Biedler, L. Helson, *et al.*, "Morphology and growth, tumorigenicity, and cytogenetics of human neuroblastoma cells in continuous culture," Cancer Res. **33**(11), 2643–2652 (1973).
30. L. Helson, L. Helson, S. K. Das, *et al.*, "Human neuroblastoma in nude mice," Cancer Res. **35**(9), 2594–2599 (1975).
31. C. D. Wijetunge, I. Saeed, B. A. Boughton, *et al.*, "A new peak detection algorithm for maldi mass spectrometry data based on a modified asymmetric pseudo-voigt model," BMC Genomics **16**(S12), S12 (2015).
32. M. A. Cardinali, S. Caponi, M. Mattarelli, *et al.*, "Brillouin scattering from biomedical samples: the challenge of heterogeneity," J. Phys. Photonics **6**(3), 035009 (2024).
33. L. Brechet, V. Gilet, N. Bouhlel, *et al.*, "Brillouin spectra simulator," figshare (2025), https://doi.org/10.6084/m9.figshare.28788665.